Precision modeling of the IBA Universal Nozzle double scattering mode at the University Proton Therapy Dresden

Lutz, B.; Eulitz, J.; Haneke-Swanson, R.; Enghardt, W.; Lühr, A.;

Originally published:

March 2021

Journal of Instrumentation 16(2021), T03007

DOI: https://doi.org/10.1088/1748-0221/16/03/T03007

Perma-Link to Publication Repository of HZDR:

https://www.hzdr.de/publications/Publ-31473

Prepared for submission to JINST

Precision modeling of the IBA Universal Nozzle double scattering mode at the University Proton Therapy Dresden for Monte Carlo simulation

B. Lutz,[a,1] **J. Eulitz,**[b,c] **R. Haneke-Swanson,**[d] **W. Enghardt,**[b,c,e] **and A. Lühr,**[b,c,f]

[a] *Helmholtz-Zentrum Dresden - Rossendorf, Institute of Radiation Physics, Dresden, Germany*

[b] *Helmholtz-Zentrum Dresden - Rossendorf, Institute of Radiooncology, Dresden, Germany*

[c] *OncoRay – National Center for Radiation Research in Oncology, Faculty of Medicine and University Hospital Carl Gustav Carus, Technische Universität Dresden, Helmholtz-Zentrum Dresden - Rossendorf, Dresden, Germany*

[d] *Ion Beam Applications SA, Chemin du Cyclotron 3, 1348 Louvain-la-Neuve, Belgium*

[e] *Department of Radiation Oncology, Faculty of Medicine and University Hospital Carl Gustav Carus, Technische Universität Dresden, Dresden, Germany*

[f] *Department of Medical Physics and Radiotherapy, Faculty of Physics, TU Dortmund University, Dortmund, Germany*

E-mail: b.lutz@hzdr.de

Abstract: Monte Carlo (MC) simulations are indispensable for many research and advanced clinical questions in proton therapy (PT). However, the necessary site-specific modeling of a double scattering (DS) PT system is extensive and challenging and requires a clear strategy. This work describes a comprehensive method for precise and accurate modeling of a DS nozzle that minimizes additional measurement effort. A detailed model of the IBA universal nozzle is created within the TOPAS simulation framework. This model is subsequently fine-tuned using a step by step procedure to match the same dose profiles used for the commissioning of the treatment planning system. In the proposed bottom-up approach, the geometry of beam-shaping elements is first adjusted to measured quantities and then the beam and model properties are optimized using iterative methods. The resulting dose distributions are validated with a set of independent measurement data to estimate the achieved quality. The resulting simulated dose distributions agree well with the data and show residual range differences of maximum 0.6 mm. The shape of the SOBP plateau regions is accurately reproduced with a spread of the residuals below 1% (i.e., near to the statistical limit) over a large part of the machine settings. The simulated lateral dose profiles, although not directly included in the optimization, match the shape of the validation data better than 0.14 mm. The minimal measurement effort and high-precision proton field modeling make this method attractive, in particular, for retrospective beam modeling needed in clinical outcome or relative biological effectiveness studies after DS treatment.

Keywords: Algorithms and Software for radiotherapy, Models and simulations, Microdosimetry and nanodosimetry

[1]Corresponding author.

Contents

1 Introduction

Proton therapy is an important modality in radiation oncology as its unique physical properties allow to minimize dose to healthy tissue while achieving highly conformal tumor target coverage. However, protons, as heavy charged particles, stop and scatter within the patient and make dose calculation in proton therapy particularly challenging compared to conventional photon therapy. The gold standard of dose calculations in proton therapy is the Monte Carlo method (MC) as it maps the stochastic nature of proton scattering and stopping most precisely [1]. MC simulations can

provide more information about various physical processes induced by the radiation than analytical algorithms. Thus, they are indispensable for many medical physics research questions.

Recently, there is an intensive debate on the variability of the clinical relative biological effectiveness (RBE) [2–4]. Considerable efforts are made to correlate early and late radiation responses that have been observed within the last five to ten years with the delivered proton radiation [5–9]. This requires an accurate and systematic retrospective simulation of large patient cohorts treated during the last decade. Besides dose, the simulation of beam quality parameters (e.g., linear energy transfer) is an essential input for RBE and normal tissue complication probability modeling as well as for the biological optimization of proton plans [10].

There are mostly two techniques in clinical use to generate laterally extended proton treatment fields from the initial mono-energetic pencil beam leaving the accelerator: pencil beam scanning (PBS) and passive scattering (PS). In PBS, the target volume is scanned using a large number of single Bragg peaks of varying energy which are deflected with dipole magnets. In PS, the initial beam is laterally scattered via a combination of scatter elements with optimized geometrical shapes. The often used combination of two scatterers is referred to as double scattering (DS). The longitudinal field extension is achieved by ridge filters or range modulator wheels (RMW). The creation of a MC simulation model for a clinical double scattering nozzle requires the implementation of all the beam shaping components.

Several groups have implemented PS systems in MC simulation [11–15]. The accuracy of the simulations depends on how well the beam generation and delivery are duplicated. Most work reported in literature uses manufacturer blueprints to model the parts of the nozzle directly relevant for the proton field shape [11–13, 15]. But, this alone is insufficient for most use cases as the simulation should rather model the actual radiation field than the design field of the machine. Most importantly, there are machining tolerances that lead to various deviations of the real components compared to the design. Consequently, the manufacturers have to introduce adjustable parameters to meet the beam specifications at each treatment site. These parameters allow to compensate for manufacturing tolerances and enable the operators to readjust a machine to always generate identical fields in case of component replacements. At the same time, these intentional degrees of freedom lead to a multitude of possible machine settings that result in a distinctive radiation field for each treatment place. Therefore, recreating the radiation fields specific to a certain treatment place requires to understand the origin of these variations and how to include them in the simulation.

The possibility to adjust the simulation and the achievable precision also depend on the availability of suitable measurements of the actual treatment field. Such measurements are time consuming and interfere with patient treatment. Therefore, the amount of required input data plays a significant role for the practicability of an optimization method.

The scattering nozzles by IBA are used at many different proton therapy centers and several optimization techniques for their simulation have been presented in the literature. The optimization of the proton beam properties at the entrance of the beam delivery system is described in [12]. That the beam current modulation can be used to match the plateau region of the spread out Bragg peak (SOBP) was demonstrated in [16]. The adjustment of the starting point on the RMW has been reported in [17]. Similar approaches are described in [15, 18]. While there is overlap between the described distinct procedures, a comprehensive approach that covers all aspects of a site specific adjustment would be highly desirable.

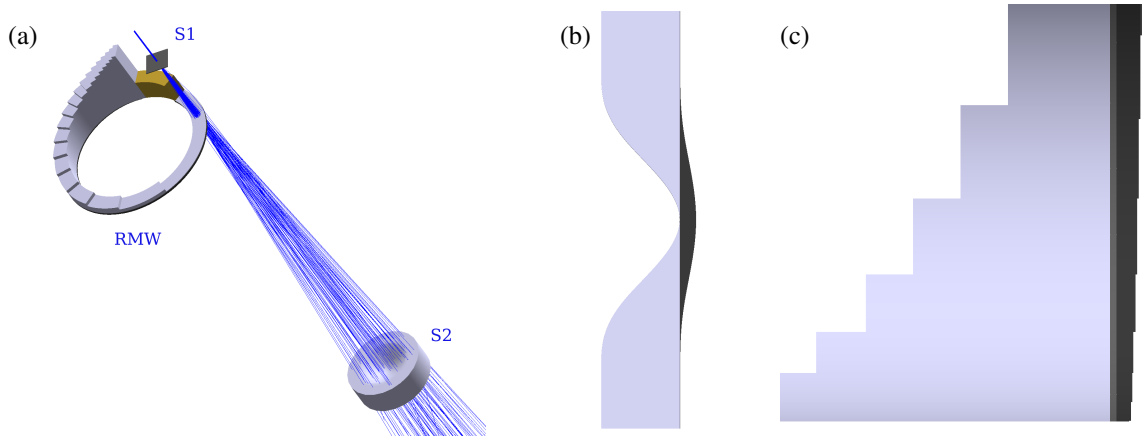

Figure 1. Implementation of double scattering (DS) in the IBA universal nozzle. Parts made of lead, plastic, and aluminum are colored in black, light gray, and dark grey, respectively. (a) Sketch of the first scatterer (S1), one track of the range modulator wheel (RMW), and second scatterer (S2) arrangement. Lines show 100 simulated protons passing through the DS system. (b) Cross section of the S2. (c) Side view of the RMW (not to scale). The plastic (low-Z material) and lead (high-Z) steps are shown on the left and right, respectively. The steps sit on the two sides of an aluminum disk depicted in dark gray.

This work describes a comprehensive method for achieving a precise and accurate modeling of the IBA universal nozzle operated in passive DS mode. It focuses on how to assess and implement site-specific parameters of such a system in a simulation using a step-wise procedure. Additionally, the method tries to minimize the number of dedicated measurements required as input for the optimization by reusing existing data sets such as the data recorded to commission the treatment planning system (TPS). This makes it especially suitable for the setup of retrospective studies.

2 Methods

The University Proton Therapy Dresden (UPTD) utilizes a treatment system manufactured and operated by Ion Beam Applications SA (IBA, Louvain-la-Neuve, Belgium). The system features a 360 degree rotating gantry and an IBA universal nozzle in a single treatment room. The universal nozzle can be operated in single scattering, DS, or PBS mode. For this work, we discuss only the operation in DS mode.

2.1 Double scattering implementation in the IBA universal nozzle

In general, a DS system consists of a flat first scatterer (S1) that widens the Gaussian lateral beam distribution and a second scatterer (S2) with a radially varying scattering power to flatten the lateral beam distribution. Figure 1(a) illustrates how protons pass through the implemented DS mode of the IBA universal nozzle; a combination of a S1, RMW, and contoured S2. A description how such a DS system works and how the necessary dimensions can be calculated can be found in [19]. The specific implementation of IBA uses a contoured S2 made of two materials as shown in figure 1(b). A high-Z material is used to define the radially varying scattering power. A second, low-Z material homogenizes the radial variation of the energy loss in the S2 to avoid a lateral variation in proton range.

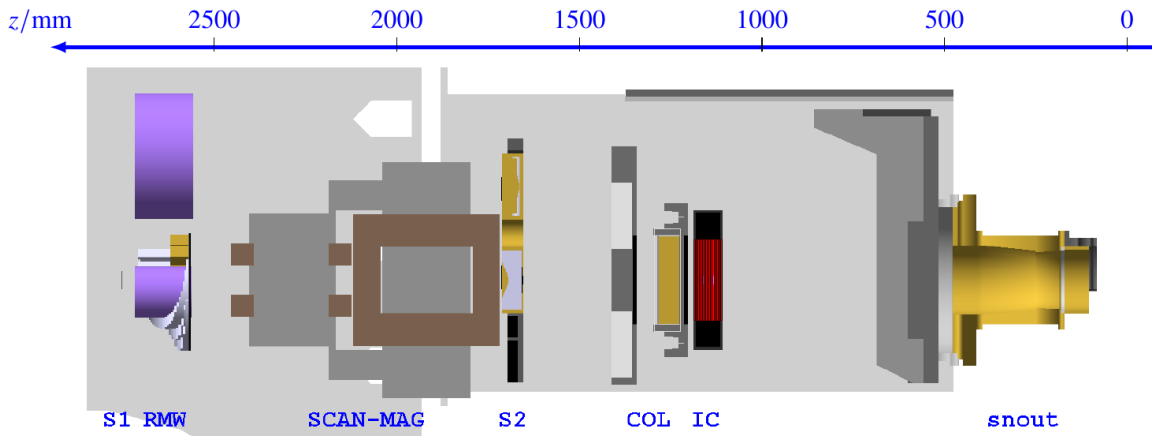

Figure 2. Cross-section of the geometrical model of the IBA universal nozzle. Protons enter the nozzle from the left and pass through the first scatterer (S1), the selected range modulator wheel (RMW), the two scanning magnets (SCAN-MAG), the second scatterer (S2), the two collimators (COL), and the ionization chamber (IC). The protons exit the nozzle through the snout that has placeholders for patient specific apertures and a range compensator. The snout sits on a movable structure that allows the adjustment of the distance between patient and beam exit. Structural parts that enclose the different components are shown in light gray. The scale shows the distance from the ISO center of the rotating gantry.

To extend the radiation field in longitudinal direction, the IBA nozzle contains a RMW that rotates at constant speed through the beam. The RMW consists of steps of increasing height, which reduce the range of the passing protons in proportion. Consequently, each step generates a Bragg peak of a certain depth in water. The width of the steps is chosen such that the statistics of the individual Bragg peaks superimpose to a flat SOBP. The steps are made from a low-Z material to minimize the additional scattering and sit on an aluminum carrier disk. Additionally, each low-Z step is complemented by a small high-Z step to keep the scattering power constant over the full wheel rotation. Figure 1(c) displays the sandwich structure of this arrangement. The RMW adds scattering and is therefore placed near to the dedicated S1 foils. In combination, they act as a virtual S1 and provide together the required scattering power of a S1 in the DS system.

A DS system works only optimal for one specific proton energy, due to the energy-dependent scattering and energy loss of protons. Therefore, the IBA universal nozzle combines 6 S1, 5 range modulator tracks, and 3 S2 to provide DS for proton ranges from 4.6 g/cm^2 to 28.4 g/cm^2. The overall range is divided into 8 major range intervals, called options. For each option, a specific combination of range modulator track and S2 is defined. Within each option, the combination of S1 depends on the selected range. Additionally, each option has 3 sub ranges that use different BCM patterns to achieve more flat SOBPs. The length of the SOBP plateau, i.e. the modulation, is adjusted by switching the beam off before the RMW completes a full rotation. More detailed descriptions of similar IBA nozzles can be found elsewhere [11, 13, 18].

2.2 IBA universal nozzle model

A simulation model of the IBA universal nozzle installed at UPTD is implemented using the TOPAS software platform [20] as a simulation framework. All simulations have been performed with TOPAS version 3.0p1 and the default physics settings. Figure 2 shows a cross section through

the geometrical model. All components have been constructed using information from the original manufacturer blueprints. Components that directly interact with the beam such as the scatterers, the RMWs, or the ionization chamber have been recreated to the smallest known details. Elements that constrain the proton path like collimators, snout, and the structural parts of the assembly are implemented with less details, but ensuring that the aperture is matched correctly. Additionally to all DS components, the PBS magnets are included as these significantly restrict the aperture between range modulator and S2. The model allows for the simulation of time-dependent aspects of the nozzle such as RMW rotation and BCM [21].

2.3 Measurements of the dose distribution and their simulation

For the commissioning (section 2.4) and validation (section 2.5) of the model, the simulated and measured data have to be compared. All dose distributions shown in this work have been measured with ionization chambers in an IBA blue phantom 2. This water phantom provides a scanning system that can position the ionization chamber with a relative precision of 0.1 mm in three dimensions [22]. Different ionization chambers are used for longitudinal and lateral measurements. The depth dose distribution is measured with a PTW Advanced Marcus Chamber (0.02 ccm). The lateral dose distribution is measured with a PTW Dosimetry Diode PR with an active volume of 1 $mm^2 \times 40\ \mu m$. The beam is directed into the phantom from the top to avoid that the beam passes a wall of the phantom. The ionization chambers are manually aligned to the water surface and a precision better than 0.3 mm is typically achieved. Each measured curve corresponds to a single scan.

A careful design of the scoring volumes in simulation is important to avoid a bias of the results, especially in regions with a steep slope like the distal or lateral edges. It would be ideal to score the dose in a volume identical to the sensitive volume of the measurement. Due to the very small sensitive volumes, this is prohibitive due to the computing power necessary to reach a reasonable statistical accuracy. Therefore, bigger bin sizes have to be chosen for the simulation and the resulting values will represent an average over this bigger volume.

In case of the depth profile, the dose is scored in a cylinder with the same diameter as the ionization chamber active volume diameter. A longitudinal bin width of 0.5 mm is a good compromise between statistical accuracy and bias due to the integration over a volume larger than in the measurement. To keep this bias to a minimum, the bin centers of the simulation are aligned with the measurement positions.

The lateral dose profile was scored in cubes of 0.5 mm edge length. The centers of the cubes were aligned with the measurement positions.

2.4 Commissioning of the simulation model

The model generated from the blueprints represents the reference design of the IBA universal nozzle. The real life nozzle differs significantly from this idealized representation. Materials are produced with slightly fluctuating densities and processing tolerances inevitably lead to variations in the physical dimensions of the components. This makes it necessary to have adjustable parameters in the design. These parameters need to allow for enough freedom so that the operators can optimize the proton field shape to fulfill clinical requirements and reproduce the once established reference field after component exchanges.

Table 1. Machine parameters that affect the proton field shape. Three different types are distinguished: manufacturing tolerance, machine specific setting, and beam quality. The column method specifies whether the treatment place-specific adjustment was done based on measurement or through optimization. The used data sources are either data sets recorded for the setup of the TPS, which contain the first pristine Bragg peak (PP1) and the spread out Bragg peak (SOBP), or measurements done by the manufacturer or the user.

Name	Type	Affects	Variability	Method	Data source
1st scatterer thickness	tolerance	range	6	meas	manufacturer
2nd scatterer composition	tolerance	range	3		
RMW composition	tolerance	range, SOBP flatness	5		
component spacing	setting	field shape	fixed	meas	user
RMW start angle	setting	modulation	5	opt	SOBP
beam current modulation	setting	SOBP flatness	3×8	opt	SOBP
beam energy offset	setting	range	8	opt	PP1
beam energy spread	beam	distal edge	energy	opt	PP1
beam width	beam	field shape	energy	meas	manufacturer

The production variations combined with the selected operational parameters lead to a treatment place specific proton field shape. A good simulation, similar to a TPS, has to reproduce this characteristic field. Consequentially, the data sets recorded to adjust the TPS can be reused to commission and validate the simulation.

This section describes the parameters that influence the proton field shape and methods how these can be inferred from different sources. Table 1 summarizes the relevant parameters and how they are treated in this work. Figure 3 sketches the procedure in form of a flowchart. The details of this procedure are described in the following paragraphs.

2.4.1 Adjustments from measurements

The first step after creating the geometrical model from blueprints is the adjustment of the nominal dimensions using measured values wherever possible. The manufacturer measures several parameters during the setup of the machine, e.g., the water equivalent thickness (WET) of the six S1 sheets allowing for the calculation of their actual thickness. This modification of the S1 is especially important as the relative manufacturing tolerances on such thin sheets are rather large. Additionally, the number of combinations is much higher than the available reference data points for the full field. This makes it impossible to optimize the properties of the first scatter from field measurements.

The situation is different for the S2 and RMW manufacturing tolerances, as these are composed of several materials. While measurements of the WET of the S2 and the first step of the RMW exist, it is unclear to which of the materials potential differences should be assigned. Therefore, these are ignored in this step. Instead, the resulting effects on the range and scattering are expected to be compensated during the later optimization of the option-dependent energy offset and the beam energy spread.

The only dedicated measurement done for this work is a measurement of the distances between the components and the absolute position towards the iso-center. This is necessary, as the position in beam direction can be adjusted for components such as the RMW which is not reflected in the technical drawings. The beam width at the entrance to the nozzle, also provided by the manufacturer,

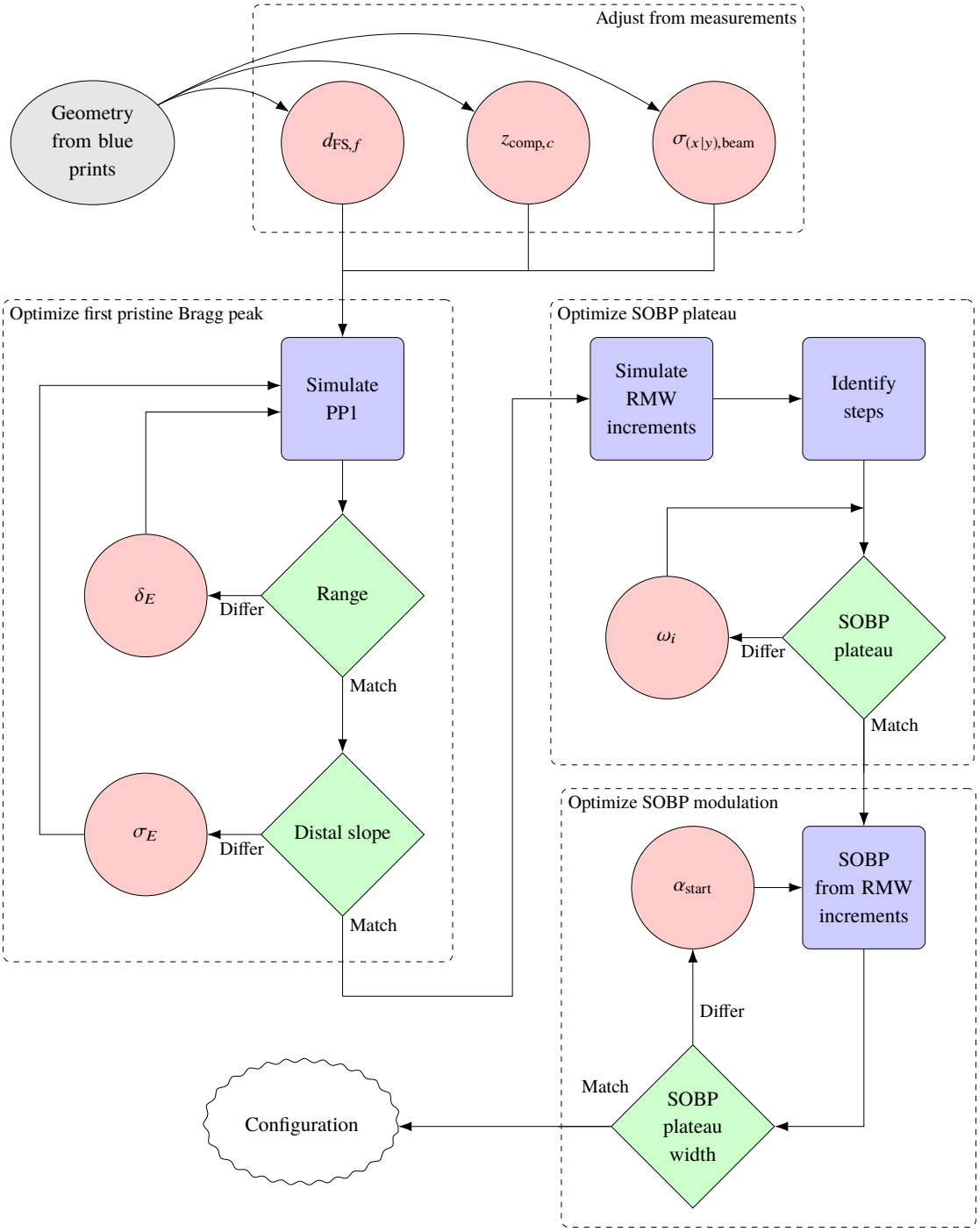

Figure 3. Flowchart of the optimization procedure to modify the simulation configuration generated from blueprints to match the treatment place. First, the thickness $d_{\mathrm{S1},f}$ of each of the six first scatterer foils, the longitudinal position $z_{\mathrm{comp},c}$ of each component c, and the spatial width of the beam $\sigma_{(x|y),\mathrm{beam}}$ in x and y direction are adjusted from measurements (section 2.4.1). Then, the beam energy offset δ_E and beam energy spread σ_E are optimized using the measurements of the first pristine Bragg peak (PP1) (section 2.4.2). Subsequently, the range modulator wheel (RMW) step weights ω_i are derived by fitting the shape of the spread out Bragg peak (SOBP) plateau (section 2.4.3). Finally, the beam start angle α_{start} on the RMW is adjusted (section 2.4.4).

has no strong influence on the field shape [16]. However, the use of an unrealistic initial beam width parameter might lead to artifacts from neighboring tracks when the beam is not contained on a single range modulator track.

2.4.2 Optimization of the pristine Bragg peaks

The data set recorded for the commissioning of the TPS contains the dose distribution of the first pristine Bragg peak (PP1) for each of the 24 machine sub-options. The range and the width of the PP1 depend on the proton energy and the energy spread, respectively. Hence, these data are used to adjust the option-dependent beam energy offset δ_E and the beam energy spread σ_E.

The measured and simulated PP1 are generated by switching off the beam while it is still on the first step of the RMW. Both PP1 curves are fitted around the peak with the analytical Bragg peak function developed by Bortfeld [23] and normalized to the maximum value of the fit to avoid normalization uncertainties due to the limited number of measurement points and simulation bins.

The proton range is evaluated at the position where the dose falls to 80% after the dose maximum (R_{80}). The energy offset δ_E is iteratively adjusted in the simulation until the difference between measured and simulated range are less than 0.5 mm.

To assess the width of the peak, five additional dose points are considered: $R_{\mathrm{p},70}$, $R_{\mathrm{p},80}$, $R_{\mathrm{p},90}$, R_{90}, R_{20}. The three points that are denoted with the letter p are located on the rising (proximal) slope while the other two and R_{80} sample the falling (distal) slope. For each dose point, the separation between simulation and measurement is calculated, e.g. $\Delta R_{80} = R_{\mathrm{sim},80} - R_{\mathrm{meas},80}$. In a second step, the variation is calculated for the 3 dose points on each side of the peak as $\delta = \sqrt{\sum_i (\Delta R_i - \sum_i \Delta R_i/3)^2}$ where i runs over 20, 80, and 90 for the distal side and over p70, p80, and p90 for the proximal side. The value of σ_E is then iteratively altered in the simulation until the two δ-values reach a minimum. As a change of the peak width also affects R_{80}, the range is checked after each step and re-optimized if the deviations exceed the threshold of 0.5 mm. The loop is repeated until the three distal dose points agree within 0.5 mm with the measured value.

Afterwards, the option-dependent energy offset is calculated as the average of the three sub-option δ_E values. The optimized beam energy spread values are tabulated as function of the requested range. The actual σ_E is then interpolated between the two values derived from the measured PP1 with the nearest ranges.

2.4.3 Optimization of the SOBP plateau

An SOBP is the superposition of several pristine Bragg peaks of different range. The width of the RMW step defines the base weight of the individual peaks. On top of these base weights, the shape of the SOBP plateau is adjusted by changing the number of protons in the individual peaks. In clinical treatment, this is done by modulating the beam current during the irradiation. This beam current modulation (BCM) serves a dual purpose. It extends the range that can be covered by a single RMW track by compensating the slope that is introduced by operating away from the optimal point. Additionally, it allows to mitigate manufacturing imperfections of the RMW steps [24]. However, the simulated RMW steps are ideal without inter-step variations and, hence, the original BCM applied in treatment are unsuitable for simulation. In fact, it is possible to achieve an improved agreement of the dose distributions by adjusting the step weights in simulation to mimic the residual imperfections of the actual measured field [16].

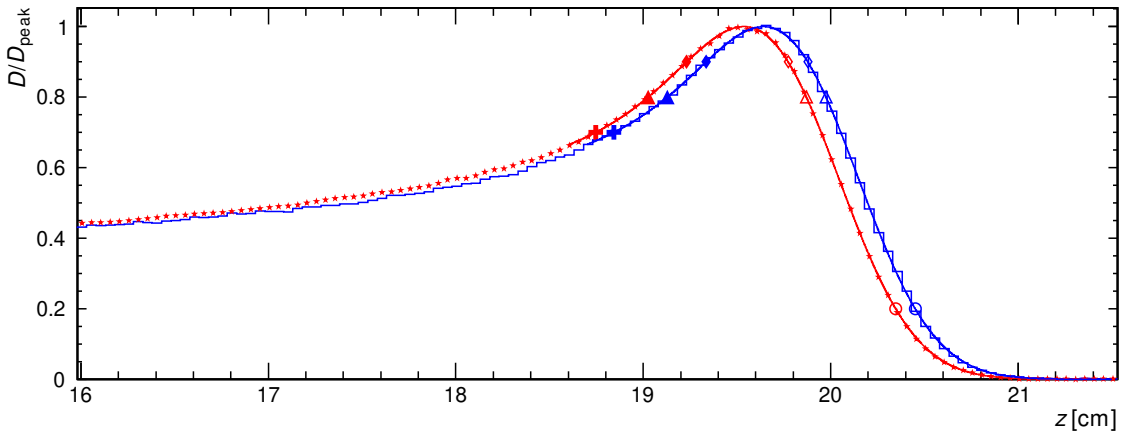

Figure 4. Measured (red stars) and simulated (blue histogram) dose distribution of the first pristine Bragg peak (PP1) before optimisation of range and width. The lines show the result of fits with the Bortfeld function. The dose points used in the evaluation of the range and width of the distribution are marked with the following symbols: $R_{p,70}$ full cross, $R_{p,80}$ full triangle, $R_{p,90}$ full diamond, R_{90} open diamond, R_{80} open triangle, and R_{20} open circle.

The TPS commissioning data set contains records of the dose profile for SOBPs of different plateau modulation widths, which are measured in the same configuration like the PP1. For each of the 24 sub-ranges, all employing individual BCM functions, one dose profile with the maximum allowed plateau modulation width is recorded. This dose profile is recreated in simulation with the scoring configuration described in section 2.3. Within this simulation, the RMW rotation is subdivided into 256 increments of 1.4 degree, which is the granularity of the accelerator BCM. This choice is made to match the accuracy of the beam off position in simulation with the one in a clinical treatment. This high angular resolution is also necessary to include the transition of the beam spot over the RMW step edges. But, it is not suitable for the optimization of the step weights. Due to the idealized model of the RMW track, all simulation points where the beam spot falls fully onto one step give indistinguishable results and consequently do not form a linear independent base. Therefore, it is necessary to combine all points from one RMW step before the weights can be optimized. A simple method to identify the step edges in the simulated data is to look at the change in the Bragg peak range versus the rotation increment. This is illustrated in figure 5. The angular ranges of the steps are in principle also known from the design, but using the simulation data avoids inconsistencies.

After the identification of the step edges, the dose versus depth histograms are summed up for each RMW step. These histograms represent the pristine Bragg peaks and form a suitable base for the optimization procedure. Subsequently, the dose distributions of the individual Bragg peaks are summed bin by bin applying one weight per RMW step. The dose D_j in a given range bin j is then given by

$$D_j = \sum_i \omega_i D_{i,j}, \tag{2.1}$$

where ω_i is the weight for the given RMW step i and $D_{i,j}$ the dose of bin j in the dose histogram

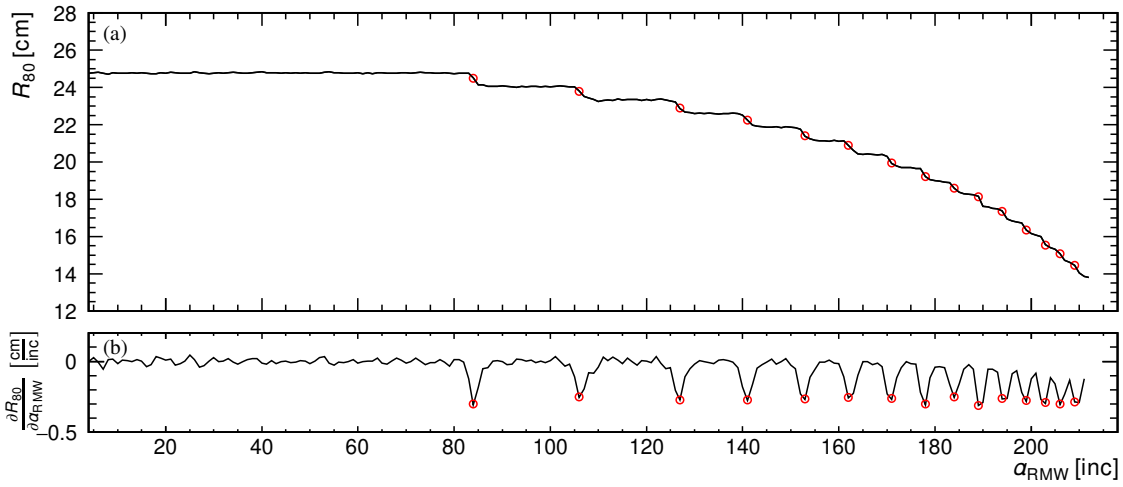

Figure 5. (a) Bragg Peak range R_{80} as a function of the range modulator wheel (RMW) angle α_{RMW}. The red circles indicate the position of the identified step edges. (b) Derivative of R_{80}. The RMW step edges can be derived from the peaks. The identified positions are marked with red circles.

of the RMW step i. This allows to use a standard χ^2-fit to match the simulated to the measured dose distribution and extract the ω_i that are used to construct the BCM-function in simulation. To increase the stability of the procedure, the fit range is restricted to the plateau region between R_{min} and R_{80}. Best results are achieved with an individual selection of R_{min} around the proximal 90% dose point. Figure 6 shows the pristine Bragg peaks and the simulated dose distribution before and after the fit procedure for one of the machine options.

2.4.4 Optimization of the plateau width

The width of the SOBP plateau is determined by the requested modulation parameter M_{req}. It controls the angular position where the beam is switched off during one RMW rotation. The angular position α_{start} where the beam switches on is one parameter that has to be adjusted by the operators during machine commissioning. In consequence, this leads to a RMW track-dependent offset between the actual plateau width and M_{req}.

To include this offset into the simulation, the dose profile using the angular resolved simulation data from section 2.4.3 is used. The curve that corresponds to a certain M_{req} smaller than the maximum are created by summing the increments in the associated range and compared to the ones recorded for TPS commissioning. Then, the number of increments that have to be removed or added to match the plateau width are estimated. The result is translated to α_{start}. It should be noted that it will be necessary to re-optimize the last step weights in case a positive offset is found.

2.5 Validation of the simulation

The simulation configuration is optimized on data points that are chosen to cover all major variations expected in the radiation fields generated by an IBA universal nozzle. However, these measurements represent only a small sample of the phase space of possible radiation fields the system can generate. Therefore, it is important to validate the results with independent measurements to ensure that the

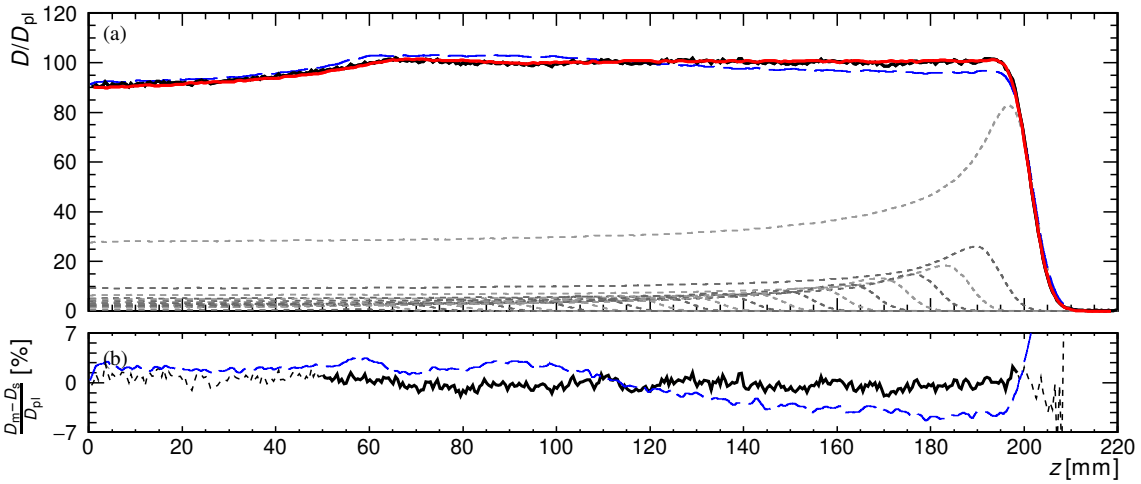

Figure 6. (a) Simulated SOBP dose distribution before (blue dashed line) and after optimization (black line) of the pristine Bragg peak weights. The red line shows the measured SOBP shape. The individual Bragg peaks are indicated as dashed gray lines. (b) Residual between the simulated and measured dose distribution. The blue dashed line shows the deviations before the optimization. The deviations after optimization are depicted with a line of black color. The line is drawn solid in the range used for the weight optimization, otherwise a dashed line is used.

simulation model represents all possible requested range R_{req} and modulation M_{req} combinations. Such a data set already exists since it is required for TPS validation, too.

The validation data set contains both depth dose curves and lateral dose profiles. For this work, one depth dose curve with medium modulation length is evaluated for each of 24 sub-options. The lateral dose profiles are compared for two different M_{req} in each of the eight options. Depending on the size of the SOBP plateau, the lateral dose profile is sampled at three or four different depths.

2.5.1 Depth dose profile

To validate the depth dose profile, the simulated and the measured data sets are normalized to the average dose in the region between $R_{\mathrm{req}} - 0.6 \cdot M_{\mathrm{req}}$ and $R_{\mathrm{req}} - 0.25 \cdot M_{\mathrm{req}}$. For each curve, the depths of the dose points $R_{\mathrm{p},98}$, R_{90}, R_{80}, and R_{20} are identified as shown in figure 7 (a) and differences between measurement and simulation are calculated. The difference at the 90% points, ΔR_{90}, is taken as measure for the range difference. The difference in modulation ΔM is calculated, where $M = R_{90} - R_{\mathrm{p},98}$. To understand if the slopes of the two curves match, the three ΔR values are plotted at -1, 0, and 1 abscissa and the slope s_{dist} between the range differences is calculated.

The success of the SOBP plateau optimization is validated in the depth interval between $R_{\mathrm{req}} - 0.9 \cdot M_{\mathrm{req}}$ and $0.95 \cdot R_{\mathrm{req}}$. This choice excludes the regions of the proximal and distal slope where differences are dominated by the separately measured range shift and do not corroborate shape differences. The residual between the two curves is calculated in the given depth interval, and filled into a histogram. The resulting distribution is then fit with a Gaussian. The width σ_{pl} of the Gaussian indicates how well the simulated curve matches the measured.

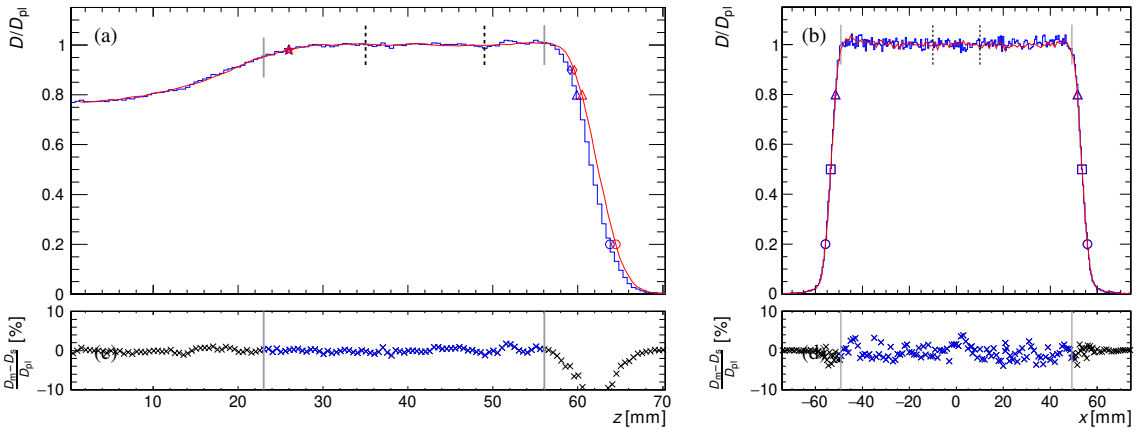

Figure 7. Validation of the depth dose distribution (a) and the lateral field shape (b). The blue histograms show the simulated field shape. The measured data are displayed by a red line. Each data set is normalized to the average value in the range between the vertical dashed black lines. Gray solid lines indicate the boundaries of the plateau regions. The markers indicate the different dose points used to evaluate the distal and lateral shapes: 20% (circle), 50% (square), 80% (triangle), 90% (diamond), and 98% (star). Blue and red markers belong to simulated and measured data, respectively. The residual between simulated and measured data is shown as crosses in (c) and (d). The residual points that are within the plateau region, indicated by blue color, are used to evaluate the plateau flatness.

2.5.2 Lateral dose profile

The lateral dose profiles are normalized in the range -1 cm to 1 cm before the 20%, 50%, and 80% dose points are identified on both lateral slopes (Figure 7 (b)). The widths W_{20}, W_{50}, and W_{80} are calculated as the difference between the corresponding right and left dose points. Furthermore, the penumbra P=x_{80}-x_{20} is calculated as a measure for the steepness of the slopes.

The lateral plateau region is defined as the range where the normalized dose is above 98% in the measured data. Analogously to section 2.5.1, the spread σ_{pl} in the plateau region is calculated for the lateral profile too.

2.5.3 Estimation of the statistical uncertainty

It is important to know the statistical uncertainty of the measurements and simulations to interpret the size of σ_{pl} described in section 2.5.1 and section 2.5.2. These can be estimated from the data if a suitably smooth section can be identified. For example, the region before the plateau is a good candidate in the case of the depth dose profiles. Here, the shallow parts of the individual Bragg peaks superpose to a function with moderate curvature and without structure. Such a shape can be well described by a polynomial function. Then, the differences between the measurement points and the fitted function should be of purely statistical nature and their spread is a good estimate for the statistical resolution σ_{stat}.

In the case of the depth dose profile, the region between 5 mm and $0.7 \cdot (R_{\mathrm{req}} - M_{\mathrm{req}})$ is fitted with a polynomial function of 3rd degree. The distribution of the residual from all fields is then fitted with a Gaussian function to extract σ_{stat}. In the case of the lateral dose distribution, σ_{stat} is extracted in a similar way, but in the range from -10 mm to 10 mm. The center of the plateau might

exhibit a slight curvature, but as long as one stays away from the field edges it is sufficiently smooth. In both cases, these procedures are done separately for the simulated and measured curves.

3 Results and Discussion

3.1 Required data

Table 1 lists the relevant parameters that have, apart from the blueprints, an influence on the actual field shape and the data sources from which these parameters can be derived. At an operating proton therapy center, most of these data are already available. The WET of the S1 and the beam width at the nozzle entrance are measured during machine setup and can be provided by the manufacturer. The depth dose distributions used in the optimization procedure are measured for the commissioning of the TPS. Here, only a subset of the depth dose distributions available at UPTD was used: the PP1 and the SOBP with maximum modulation for each of the 24 sub-options to model the field shape, and three SOBP with shorter than maximum modulation for each of the eight options to identify the start angle. The determination of the geometrical distances between the components of the nozzle (i.e., the only measurement) was performed parasitically during a regular maintenance slot of the accelerator. In consequence, the described method can be performed without any impact on patient treatment.

3.2 Evaluation of depth dose profile

Figure 8 summarizes the results from the comparison of simulated and measured depth dose curves. Two data sets are evaluated. First, the residual differences between reference data and simulation are shown. Second, the quality of the simulation is validated at machine settings not used during optimization.

3.2.1 Range

The residual range differences between the reference data and the optimized simulation are within ±0.3 mm for all except 2 range settings (figure 8 (a)). Only in option 8, the differences between the three values from the sub-ranges exceeded 0.5 mm. Therefore, the option-dependent energy offset for this option was calculated as an average of the two closer values. This is done to avoid an eventual bias due to a potentially bad measurement in one of the sub-ranges. The maximum deviation of 0.7 mm is then found for the excluded value.

The results from the validation data break up into two distinct classes. The deviations in options 6 to 8 are of similar size as found for the reference data. This indicates a very good modeling of the different nozzle components and, thus, that the results can be extrapolated. The results for options 2 to 5 show a clear negative offset between simulation and measurement. To understand the source of this deviation, commonalities between these machine options and between the measured data sets have been investigated. Different range modulator tracks and S2 are used in these options. Some of these tracks and scatterers are also used, in different combinations, in the unaffected options. Therefore, their modeling can be excluded as the source of the observed deviation. The reference data were measured in several individual measurements performed on different days. This makes a common bias in the input data to the optimization unlikely. The only connection that could be

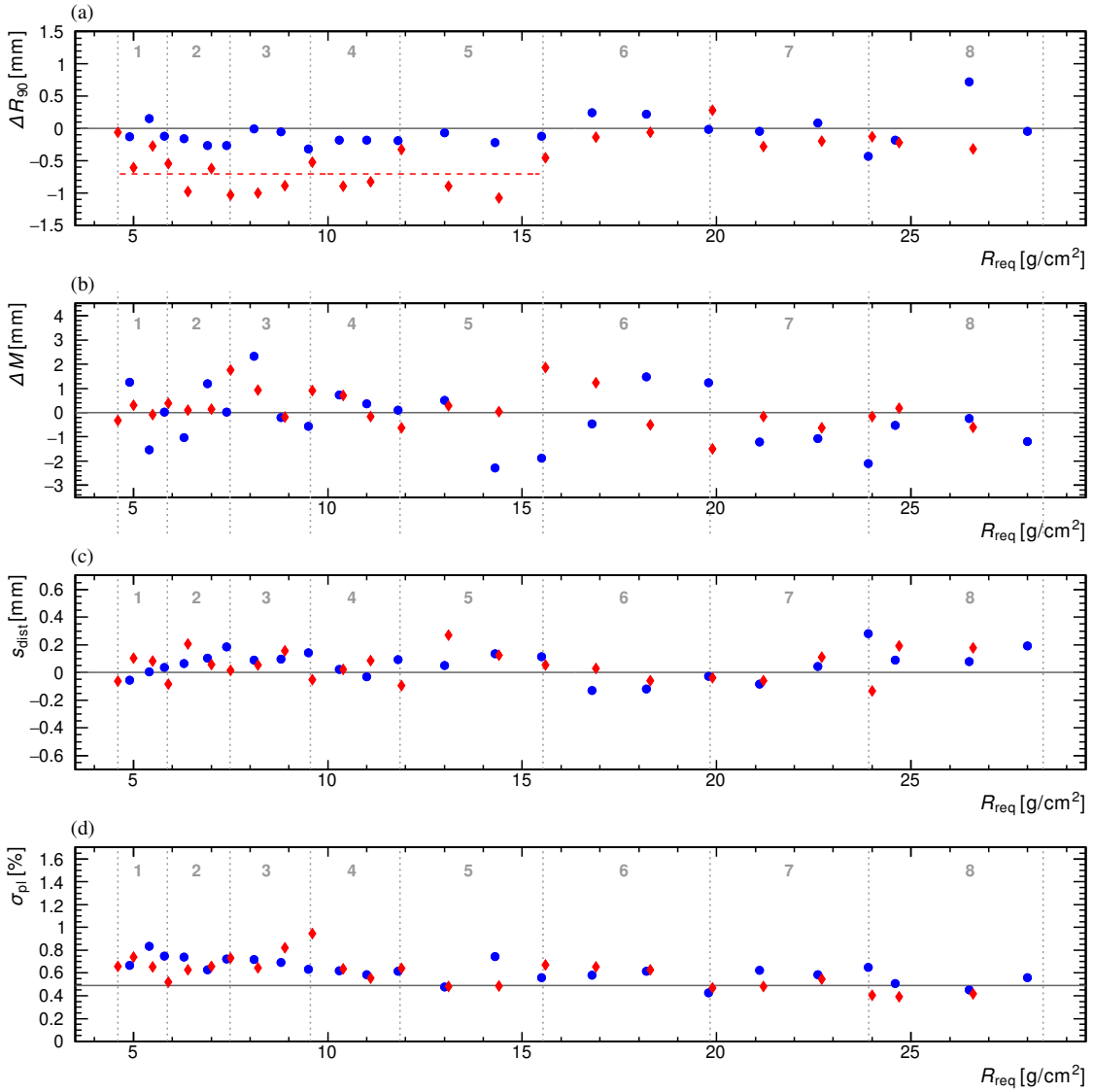

Figure 8. Results for the depth dose profiles. Deviations between simulated and measured data of R_{90} (a), M (b), s_{dist} (c), and σ_{pl} (d). Blue circles show the reference data used to optimize the model. Red diamonds show the independent validation data. The gray numbers and vertical lines indicate the ranges of the eight double scattering options. The solid horizontal lines indicate the ideal value. The dashed red line in (a) indicates the average shift of R_{90} for option 1 to 5.

identified is that the validation data for options 1 to 5 were all collected in a single measurement campaign spanning one shift. Therefore, a bias in the validation measurements seems to be the most likely cause for the observed range shift. The average shift of R_{90} for options 1 to 5 is 0.7 mm. Using this shift as an alternative reference for the first five options, the matching of the range is typically better than 0.3 mm with only two settings exceeding this value and a maximum deviation of 0.6 mm. The bias in the validation data set should be verified with additional measurements. Nevertheless, even without the baseline shift for options 1 to 5, the maximum observed deviation

of 1.1 mm is still sufficient for many applications.

3.2.2 Modulation

The simulated modulation matches the measured within 2.5 mm for the reference data and better than 2 mm for the validation data. The difference in the two data sets is due to their different modulation width. The reference data is recorded with the maximum modulation setting. The validation data uses shorter SOBP widths. Two effects make it harder to get exact results for longer modulations. First, the BCM weights are less constraint for the last BCM steps and therefore inherently fluctuating stronger. Second, the proximal slope of the curve is flatter which increases the influence of statistical fluctuations on the calculation of $R_{p,98}$.

3.2.3 Distal slope

For the distal slope, both, the reference and the validation measurements, are well modeled (figure 8 (b)) with deviations to the simulations being typically below 0.2 mm and a maximum deviation of 0.27 mm. This means that the range spread of the protons is well reproduced. It also shows that it is sufficient to only optimize the energy spread, while a separate treatment of the scattering power uncertainties of the RMW and the S2 is unnecessary.

3.2.4 Plateau region

The evaluation of the plateau shows that the shape is matched quite accurately. The combined variation in the plateau region, σ_{pl}, including methodological and statistical variation, is below 1% for all tested settings (figure 8 (c)). Furthermore, σ_{pl} is near to the statistical limit over a large part of the machine settings. The slight increase in σ_{pl} for low range settings coincides with the observation that it is more difficult to find a stable solution for the fit of the step weights (section 2.4.3). This is expected to some degree as all fields are sampled with the same spatial resolution. In consequence, dose distributions with short ranges have significantly less measurement points that constrain the fit.

3.3 Lateral dose profile

No lateral dose distributions are used in the assessment of the simulation model parameters. Therefore, the validation of the lateral field shape can be used as an independent test of the simulation model quality. The results have been studied for trends and systematic effects that indicate missing details in the geometrical description.

In general, the lateral shapes are matched very well (table 2). No significant differences between the machine options can be observed. The steep slopes at the field edges are reproduced in detail and the simulated penumbras match the measurements. Also, the plateau is perfectly matched within the statistical resolution of the method. Small but statistically significant deviations can only be observed for the field widths in the y-direction. The simulated fields are 0.14 mm wider in the y-direction than the measured ones. At the same time, the resulting differences for the x-direction are compatible with zero. This difference of the two directions comes from an asymmetry that is present in the measured field shapes which is not reproduced in the simulation. The source of this discrepancy could be due to the description of the beam at the start of the simulation, which

Table 2. Results of the lateral validation. The average values μ and the spread σ are reported for the differences of the field width ΔW, the differences in left and right penumbra ΔP_r and ΔP_l, and the spread of the differences in the plateau σ_pl. ΔW is calculated for three different dose levels: 20%, 50%, and 80% of the plateau dose. Values are shown separately for x- and y-direction.

Value	Direction	ΔW_{20} (mm)	ΔW_{50} (mm)	ΔW_{80} (mm)	ΔP_l (mm)	ΔP_r (mm)	σ_pl (%)
μ	x	-0.01 ± 0.02	-0.02 ± 0.02	-0.03 ± 0.02	0.02 ± 0.02	-0.05 ± 0.03	1.37 ± 0.04
μ	y	0.15 ± 0.02	0.09 ± 0.02	0.18 ± 0.02	-0.02 ± 0.02	0.01 ± 0.02	1.40 ± 0.03
σ	x	0.09 ± 0.02	0.11 ± 0.02	0.10 ± 0.02	0.11 ± 0.02	0.17 ± 0.03	0.24 ± 0.04
σ	y	0.14 ± 0.02	0.10 ± 0.02	0.15 ± 0.03	0.12 ± 0.02	0.09 ± 0.02	0.19 ± 0.03

Table 3. Number of simulated initial protons and simulated dose in plateau region. The factor n in the pristine Bragg peak data set indicates that these have to be simulated multiple times during the iterative procedure.

Data set	Number of configurations	Initial protons		Plateau dose (Gy)	
		min	max	min	max
pristine Bragg peaks	24 x n	0.9e9	1.2e9		
angular resolved SOBP	24	1.3e9	2.8e9	1.0e-3	2.7e-3
validation	48	3.0e8	4.8e8	2.2e-4	7.3e-4

Table 4. Measured statistical resolution of the plateau region in simulation and measurement. The third column represents the calculated combined resolution. All values are in %.

	σ_stat (%)		
	Simulation	Measurement	Combined
depth	0.46 ± 0.01	0.166 ± 0.004	0.49 ± 0.01
lateral	1.19 ± 0.04	0.70 ± 0.04	1.39 ± 0.04

is currently assumed to be symmetric and perfectly aligned with the geometrical axis. Due to its small absolute size, no further investigation of the source of the deviation has been undertaken.

3.4 Statistical resolution

Table 3 gives an overview of the extent of simulations performed for the different steps of the optimization as well as the evaluation of the results. For the validation data set, described in section 2.5, the statistical fluctuations are evaluated. The results are summarized in table 4. It should be noted that the current number of protons in the validation data set is insufficient to reproduce the precision of the corresponding measurements. Therefore, the overall resolution of the comparison is dominated by the statistical error of the simulation. Roughly 3 to 8 times more particles would have to be simulated to match the two resolutions.

The pristine Bragg peaks and the angular resolved SOBP components, which are used in the optimization procedures described in section 2.4, are simulated with an increased number of protons to avoid any limitation by statistical fluctuations in the optimization.

3.5 Comparison to previous works

The presented modeling approach was developed along the working principles of the IBA universal nozzle. Naturally, its methodology overlaps with previously reported work in this field. But, the focus on the optimization of the nozzle model makes this the most comprehensive and detailed description of such a methodology. A key difference to previously reported work is a special focus on avoiding bias by binning and normalization. The first is minimized by selecting a binning compatible with the sensitivity of the measurement devices (section 2.3). The second is averted by using a fit with the Bortfeld function to normalize the first pristine Bragg peaks (section 2.4.2), which is so far unique. Furthermore, the method tries to achieve the best matching to the measured depth dose curve by an optimization of the BCM. It is also the first work that presents an analysis of the statistical power of the SOBP shape matching.

The validation with measurements shows that the chosen strategy can improve the conformity of the simulation with the actual dose distributions compared to previous work. The range and modulation are matched with maximum deviations of 0.6 mm and 2.5 mm, respectively. The deviations in the plateau dose profile are smaller than 1%. The lateral field width is reproduced better than 0.15 mm and the penumbra agrees within the statistical resolution.

For comparison, the most extensively described IBA system is the one installed at the Massachusetts General Hospital (MGH) [11, 12, 25, 26]. The detail of their geometrical model is comparable to the one described here except that no support structures seem to be included. Also, the optimized parameter sets are comparable except that they used the actual BCM functions which they did not optimize. An agreement for range and modulation of +1-2 mm and ±3 mm, respectively, are reported. The field width and plateau are matched within ±3% [26]. Another example is the modelling of the IBA system at the National Cancer Center in Korea (KNCC) for which results have been reported [15, 27]. The setup seems very similar to the MGH setup. The achieved accuracy in range and modulation, reported for a limited number of fields, is ±0.8 mm. The dose profile is matched within ±2%. For both examples, it cannot be distinguished if the larger deviations in the flat part of the dose profile are due to differences in the optimization or due to the invested computational time as no statistical sensitivity analysis is presented.

A similar approach was followed in [28]. The reported agreement of range and modulation are 0.5 mm and 5 mm, respectively. The matching of the SOBP plateau is reported as within 2% and the lateral penumbra is matched within 0.5 mm.

Another notable difference between the presented and previous models using Geant4/TOPAS is the high level of detail of the geometrical description, which includes passive components such as housing and structural plates. This allows for extending the simulation to predict the stray radiation field dominated by neutrons [29]. Compared to simulations with the Monte Carlo N-Particle Transport eXtended software (MCNPX), this reduces the effort in model building as MCNPX does not support variable geometries. For example, a model of Proton Therapy Center of Institut Curie in France was created using MCNPX [30] to simulate the neutron field [13]. Only one point per RMW step is simulated and transitions over step edges are not included.

3.6 Relevance and perspective

The presented modeling approach facilitates the implementation of MC models in passive scattering proton therapy. These models are currently highly demanded for analyzing larger retrospective clinical PT datasets. In particular, detailed studies to precisely assess the potential impact of a variable clinical proton RBE are performed. They require, however, high-precision dose and LET simulations in patients that are based on accurate model calibration using water phantom measurements. The applicability of the presented model for retrospective clinical variable RBE studies was successfully demonstrated [7]. Besides the frequently used LET, a full MC model allows for calculating more sophisticated quantities relevant for radiobiology including the beam quality Q, which may improve the direct comparability of clinical RBE values in particle therapy with different ions [31].

The commissioned MC model has been used to implement an independent treatment verification tool to avoid additional measurements [32]. Relevant dose deviation between MC an pencil-beam based clinical TPS can occur, since pencil beam algorithms underestimate Bragg peak degradation [33] in heterogeneous patient anatomies as found, e.g., in lung tumor irradiation. Additionally, lung tumors often have a large breathing motion amplitude, which remains an important inclusion criterion for passive scattering proton therapy as a robust technique mitigating tumor motion uncertainties and interplay effects. Furthermore, the MC model improves the assessment of radiation exposure due to scattered and secondary particles produced by the interaction within the nozzle and the patient also outside of the field, which is essential for radiotherapy, e.g., during pregnancy [34].

In addition to treatment plan dose verification in patients, the presented approach has been applied to water phantom dose verification and to determine absolute dose values. This may reduce measurement effort in machine and patient-specific quality assurance and improves the cost effectiveness of passive scattering proton therapy. In particular, absolute dose measurements to obtain the field-specific monitor units for patient treatment require time-consuming measurement efforts, as they are performed separately for each treatment field. The potential of the implemented MC precision model in absolute dose prediction has been demonstrated elsewhere [32].

4 Conclusion

In this study, a comprehensive Monte Carlo modeling approach for double scattering treatments is presented. It is applied to an IBA universal nozzle within the simulation framework TOPAS. The approach compensates for manufacturer uncertainties using an iterative optimization of initial beam energy and -fluence distributions based on precise commissioning measurements in a water phantom. The resulting high precision in treatment field simulations and the minimization of the required measurement effort by reusing available commissioning data make this method attractive for modeling of double scattering treatments. Its application for independent patient treatment plan verification, biological modeling and absolute dose predictions has already been demonstrated.

Acknowledgments

Many thanks to Daniela Kunath, Julia Hytry, and Stefan Menkel from the UPTD for their assistance in understanding the reference and validation data measurements. We also thank Ion Beam Applications (IBA Inc., Louvain la Neuve, Belgium) for providing the blueprints of the nozzle and information about the material compositions. Furthermore, we would like to express our thanks to the local IBA team for answering our many questions and granting access to their measurement results. Finally, we would like to thank the Deutsches Elektronen Synchrotron – DESY for supporting us through the Matter and Technologies program with access to the DESY computer cluster. This research is funded by the European Social Fund and co-financed by tax funds based on the budget approved by the members of the Saxon State Parliament (Eulitz Jan, 100316833).

References

[1] H. Paganetti, *Range uncertainties in proton therapy and the role of Monte Carlo simulations*, *Phys. Med. Biol.* **57** (2012) R99.

[2] A. Lühr, C. von Neubeck, J. Pawelke, A. Seidlitz, C. Peitzsch, S. M. Bentzen et al., *"Radiobiology of proton therapy": Results of an international expert workshop*, *Radiother. Oncol.* **128** (2018) 56 .

[3] J. Ödén, P. M. DeLuca Jr. and C. G. Orton, *The use of a constant rbe=1.1 for proton radiotherapy is no longer appropriate*, *Med. Phys.* **45** (2018) 502 [https://aapm.onlinelibrary.wiley.com/doi/pdf/10.1002/mp.12646].

[4] H. Paganetti, E. Blakely, A. Carabe-Fernandez, D. J. Carlson, I. J. Das, L. Dong et al., *Report of the aapm tg-256 on the relative biological effectiveness of proton beams in radiation therapy*, *Med. Phys.* **46** (2019) e53 [https://aapm.onlinelibrary.wiley.com/doi/pdf/10.1002/mp.13390].

[5] C. R. Peeler, D. Mirkovic, U. Titt, P. Blanchard, J. R. Gunther, A. Mahajan et al., *Clinical evidence of variable proton biological effectiveness in pediatric patients treated for ependymoma*, *Radiother. Oncol.* **121** (2016) 395 .

[6] T. S. Underwood, C. Grassberger, R. Bass, S. M. MacDonald, N. M. Meyersohn, B. Y. Yeap et al., *Asymptomatic late-phase radiographic changes among chest-wall patients are associated with a proton rbe exceeding 1.1*, *Int. J. Radiat. Oncol. Biol. Phys.* **101** (2018) 809 .

[7] J. Eulitz, E. Troost, F. Raschke, E. Schulz, B. Lutz, A. Dutz et al., *Predicting late magnetic resonance image changes in glioma patients after proton therapy*, *Acta Oncol.* **58** (2019b) 1536 [https://doi.org/10.1080/0284186X.2019.1631477].

[8] E. Bahn, J. Bauer, S. Harrabi, K. Herfarth, J. Debus and M. Alber, *Late contrast enhancing brain lesions in proton-treated patients with low-grade glioma: Clinical evidence for increased periventricular sensitivity and variable rbe*, *Int. J. Radiat. Oncol. Biol. Phys.* (2020) .

[9] C.-C. Wang, A. L. McNamara, J. Shin, J. Schuemann, C. Grassberger, A. G. Taghian et al., *End-of-range radiobiological effect on rib fractures in patients receiving proton therapy for breast cancer*, *Int. J. Radiat. Oncol. Biol. Phys.* **107** (2020) 449 .

[10] H. Paganetti, *Relative biological effectiveness (RBE) values for proton beam therapy. variations as a function of biological endpoint, dose, and linear energy transfer*, *Phys. Med. Biol.* **59** (2014) R419.

[11] H. Paganetti, H. Jiang, S. Lee and H. M. Kooy, *Accurate Monte Carlo simulations for nozzle design, commissioning and quality assurance for a proton radiation therapy facility*, *Med. Phys.* **31** (2004) 2107 [https://aapm.onlinelibrary.wiley.com/doi/pdf/10.1118/1.1762792].

[12] H. Paganetti, H. Jiang, K. Parodi, R. Slopsema and M. Engelsman, *Clinical implementation of full Monte Carlo dose calculation in proton beam therapy*, *Phys. Med. Biol.* **53** (2008) 4825.

[13] R. Sayah, L. Donadille, A. Aubé, J. Hérault, S. Delacroix, L. De Marzi et al., *Monte Carlo simulation of a proton therapy beamline for intracranial treatments*, *Radioprotection* **48** (2013) 317.

[14] W. Newhauser, N. Koch, S. Hummel, M. Ziegler and U. Titt, *Monte carlo simulations of a nozzle for the treatment of ocular tumours with high-energy proton beams*, *Phys. Med. Biol.* **50** (2005) 5229.

[15] W.-G. Shin, M. Testa, H. S. Kim, J. H. Jeong, S. B. Lee, Y.-J. Kim et al., *Independent dose verification system with Monte Carlo simulations using TOPAS for passive scattering proton therapy at the national cancer center in Korea*, *Phys. Med. Biol.* **62** (2017) 7598.

[16] B. Bednarz, H.-M. Lu, M. Engelsman and H. Paganetti, *Uncertainties and correction methods when modeling passive scattering proton therapy treatment heads with Monte Carlo*, *Phys. Med. Biol.* **56** (2011) 2837.

[17] C. Beltran, Y. Jia, R. Slopsema, D. Yeung and Z. Li, *A simplified methodology to produce Monte Carlo dose distributions in proton therapy*, *J. Appl. Clin. Med. Phys.* **15** (2014) 2 [https://aapm.onlinelibrary.wiley.com/doi/pdf/10.1120/jacmp.v15i4.4413].

[18] M. Engelsman, H. Lu, D. Herrup, M. Bussiere and H. M. Kooy, *Commissioning a passive-scattering proton therapy nozzle for accurate SOBP delivery*, *Med. Phys.* **36** (2009) 2172 [https://aapm.onlinelibrary.wiley.com/doi/pdf/10.1118/1.3121489].

[19] E. Grusell, A. Montelius, A. Brahme, G. Rikner and K. Russell, *A general solution to charged particle beam flattening using an optimized dual-scattering-foil technique, with application to proton therapy beams*, *Phys. Med. Biol.* **39** (1995) 2201.

[20] J. Perl, J. Shin, J. Schümann, B. Faddegon and H. Paganetti, *Topas: An innovative proton Monte Carlo platform for research and clinical applications*, *Med. Phys.* **39** (2012) 6818 [https://aapm.onlinelibrary.wiley.com/doi/pdf/10.1118/1.4758060].

[21] J. Shin, J. Perl, J. Schümann, H. Paganetti and B. A. Faddegon, *A modular method to handle multiple time-dependent quantities in Monte Carlo simulations*, *Phys. Med. Biol.* **57** (2012) 3295.

[22] C. Bäumer, B. Koska, J. Lambert, B. Timmermann, T. Mertens and P. T. Talla, *Evaluation of detectors for acquisition of pristine depth-dose curves in pencil beam scanning*, *J. Appl. Clin. Med. Phys.* **16** (2015) 151 [https://aapm.onlinelibrary.wiley.com/doi/pdf/10.1120/jacmp.v16i6.5577].

[23] T. Bortfeld, *An analytical approximation of the bragg curve for therapeutic proton beams*, *Med. Phys.* **24** (1997) 2024 [https://aapm.onlinelibrary.wiley.com/doi/pdf/10.1118/1.598116].

[24] H. Lu and H. Kooy, *Optimization of current modulation function for proton spread-out Bragg peak fields*, *Med. Phys.* **33** (2006) 1281 [https://aapm.onlinelibrary.wiley.com/doi/pdf/10.1118/1.2188072].

[25] H. Paganetti, *Four-dimensional Monte Carlo simulation of time-dependent geometries*, *Phys. Med. Biol.* **49** (2004) N75.

[26] M. Testa, J. Schümann, H. Lu, J. Shin, B. Faddegon, J. Perl et al., *Experimental validation of the TOPAS Monte Carlo system for passive scattering proton therapy*, *Med. Phys.* **40** (2013) 121719 [https://aapm.onlinelibrary.wiley.com/doi/pdf/10.1118/1.4828781].

[27] W.-G. Shin, C. H. Min, J.-I. Shin, J. H. Jeong and S. B. Lee, *A monte carlo study of the relationship between the time structures of prompt gammas and the in-vivo radiation dose in proton therapy*, *J. Korean Phys. Soc.* **67** (2015) 248.

[28] H. Liu, Z. Li, R. Slopsema, L. Hong, X. Pei and X. G. Xu, *Topas monte carlo simulation for double scattering proton therapy and dosimetric evaluation*, *Phys. Medica* **62** (2019) 53 .

[29] B. Lutz, M. Reginatto, M. Zboril, M. Dommert, R. Swanson, W. Enghardt et al., *Characterisation of the secondary neutron radiation at the university proton therapy dresden*, in *2018 IEEE Nuclear Science Symposium and Medical Imaging Conference Proceedings (NSS/MIC)*, pp. 1–6, 2018.

[30] J. S. Gendricks, G. W. McKinney, J. W. Durkee, J. P. Finch, M. L. Fensin, M. R. James et al., *MCNPX, VERSION 26C*. Los Alamos National Laboratory, 2006.

[31] A. Lühr, C. v. Neubeck, S. Helmbrecht, M. Baumann, W. Enghardt and M. Krause, *Modeling in vivo relative biological effectiveness in particle therapy for clinically relevant endpoints*, *Acta Oncol.* **56** (2017) 1392.

[32] J. Eulitz, B. Lutz, P. Wohlfahrt, A. Dutz, W. Enghardt, C. Karpowitz et al., *A monte carlo based radiation response modelling framework to assess variability of clinical RBE in proton therapy*, *Phys. Med. Biol.* **64** (2019a) 225020.

[33] K.-S. Baumann, V. Flatten, U. Weber, S. Lautenschläger, F. Eberle, K. Zink et al., *Effects of the bragg peak degradation due to lung tissue in proton therapy of lung cancer patients*, *Radiat. Oncol.* **14** (2019) 183.

[34] C. Geng, M. Moteabbed, J. Seco, Y. Gao, X. G. Xu, J. Ramos-Méndez et al., *Dose assessment for the fetus considering scattered and secondary radiation from photon and proton therapy when treating a brain tumor of the mother*, *Phys. Med. Biol.* **61** (2016) 683.